

# Numerical Simulation of Hurricane Bonnie (1998). Part I: Eyewall Evolution and Intensity Changes

TONG ZHU AND DA-LIN ZHANG

*Department of Meteorology, University of Maryland, College Park, College Park, Maryland*

FUZHONG WENG

*NOAA/NESDIS Office of Research and Applications, Camp Springs, Maryland*

(Manuscript received 13 November 2002, in final form 18 July 2003)

## ABSTRACT

In this study, a 5-day explicit simulation of Hurricane Bonnie (1998) is performed using the fifth-generation Pennsylvania State University–National Center for Atmospheric Research Mesoscale Model (MM5) with the finest grid length of 4 km. The initial mass, wind, and moisture fields of the hurricane vortex are retrieved from the Advanced Microwave Sounding Unit-A (AMSU-A) satellite measurements, and the sea surface temperature (SST) is updated daily. It is shown that the simulated track is within 3° latitude–longitude of the best track at the end of the 5-day integration, but with the landfalling point close to the observed. The model also reproduces reasonably well the hurricane intensity and intensity changes, asymmetries in cloud and precipitation, as well as the vertical structures of dynamic and thermodynamic fields in the eye and eyewall.

It is shown that the storm deepens markedly in the first 2 days, during which period its environmental vertical shear increases substantially. It is found that this deepening could occur because of the dominant energy supply by a strong low-level southeasterly flow into the eastern eyewall plus the presence of underlying warm SST and favorable upper-level divergent outflow. However, the approaching of a strong upper-level northwesterly flow tends to generate mass convergence and subsidence warming and drying, thereby suppressing the development of deep convection in the western semicircle. This gives rise to wavenumber-1 asymmetries in clouds and precipitation (i.e., a partial eyewall) and the eastward tilt of the eyewall and storm center. Both the observed and simulated storms also appear to exhibit eyewall replacement scenarios in which the storms weaken as double eyewalls appear, and then reintensify as their inner eyewalls diminish and concentric eyewalls develop. The results indicate that the eyewall replacement process may be predictable because it appears to depend on the large-scale flow.

## 1. Introduction

Many earlier observations have shown the development of asymmetric clouds, precipitation, and winds in tropical cyclones. For example, Miller (1958) noted that the rainfall rates ahead of the storm center are greater than those to the rear from hourly rain gauge data for 16 landfalling hurricanes in Florida. Burpee and Black (1989) examined the radar reflectivity associated with Hurricanes Alicia (1983) and Elena (1985) and found that the maximum rain rates remain in the right-front quadrant most times. By analyzing three-dimensional (3D) Doppler winds in Hurricane Norbert (1984), Marks et al. (1992) revealed that the wind field is highly asymmetric, and the asymmetry varies with altitude, with the maximum vertical velocity located to the left of the track

at all levels. Franklin et al. (1993) analyzed the Doppler winds and radar reflectivity of Hurricane Gloria (1985) and showed that a persistent asymmetry in the eyewall convection is associated with the vertical shear of environmental flow. In a recent study, Corbosiero and Molinari (2002) examined the cloud-to-ground lightning data in 35 tropical cyclones over land and within 400 km of the coast over water. They found that under the vertical shear of exceeding  $10 \text{ m s}^{-1}$  between 200 and 850 hPa, about 93% of flashes occur in the downshear quadrant with a slight downshear-left preference.

The downshear-left asymmetric eyewall pattern has also been clearly demonstrated by idealized model simulations. Using the Geophysical Fluid Dynamics Laboratory (GFDL) hurricane model, Bender (1997) performed a series of simulations to investigate the effects of asymmetric relative flow on the generation of asymmetries in the eyewall. With an easterly vertical shear, the upward motion increases significantly in the front of the storm and decreases in the rear, and the precipitation maximum shifts to the left-front quadrant. Frank

---

*Corresponding author address:* Dr. Da-Lin Zhang, Dept. of Meteorology, University of Maryland, College Park, College Park, MD 20742-2425.  
E-mail: dalin@atmos.umd.edu

and Ritchie (1999) simulated tropical-cyclone-like vortices under different vertical wind shear environments using the fifth-generation Pennsylvania State University–National Center for Atmospheric Research (PSU–NCAR) Mesoscale Model (MM5). They found that more intense convection tends to be organized at the left side of the shear vector, looking downshear. It should be mentioned that using their terminology of downshear left/right to describe the hurricane asymmetric pattern appears to be physically clearer than using the left/right of a storm track. This is because the distribution of intense convection can change from the left to right of the storm track, depending upon easterly or westerly shear, but it is always at the downshear-left side. Recently, Rogers et al. (2003) performed a 5-day real-data simulation of Hurricane Bonnie (1998) to investigate the role of vertical wind shear in determining the distribution of rainfall. They also found the wave-number-1 and downshear-left pattern in the simulated radar reflectivity under strong vertical shear and the symmetric (asymmetric) distribution of the accumulated rainfall across the track of the storm when the shear was across (along) track.

There are several hypotheses for the relationship between vertical shear and hurricane asymmetries. With a simple slab planetary boundary layer (PBL) model, Shapiro (1983) found that the asymmetric winds in the PBL are forced by the asymmetry in frictional drag associated with the storm translation. Willoughby et al. (1984) suggested a vortex stretching and compression mechanism by which the low-level convergence and divergence could be induced as the environmental relative flow passes through the region of high relative vorticity. Specifically, as the low-level easterly flow crosses the vortex from east to west, its convergence tends to moisten and destabilize the east side of the storm, leading to deep convective development. In contrast, the low-level divergence at the west side suppresses convection through stabilization and drying of the troposphere. This hypothesis was later confirmed by Bender (1997), who performed a vorticity budget of relative flow using an idealized simulation. He found that asymmetries in convergence and divergence, vertical motion, and accumulated precipitation are all closely related to the field of vorticity stretching. DeMaria (1996) used a two-layer diagnostic balance model to study the effect of potential vorticity (PV) tilt on the thermal structure of a cyclonic vortex and found that the balanced mass field associated with the tilted PV requires an increased midlevel temperature perturbation near the vortex center. It was hypothesized that the midlevel warming reduces the convection and weakens the storm. In an idealized simulation of the extratropical transition of a tropical cyclone with the U. S. Navy Coupled Ocean–Atmosphere Model Prediction System (COAMPS), Ritchie and Elsberry (2001) noted mechanically forced subsidence resulting from the convergence between a midlatitude flow and the cyclone’s circulation. This subsidence tends to erode

gradually clouds and deep convection in the west to south sectors of the storm. Because of the relatively coarse resolution ( $\Delta x = 15$  km) they used, inner-core structures were not examined.

In this study, we will investigate the mechanism(s) by which inner-core asymmetries in flows, clouds, and precipitation develop and their relationship to hurricane intensity changes using a 5-day, high-resolution ( $\Delta x = 4$  km), real-data simulation of Hurricane Bonnie (1998) with MM5. This storm developed a partial eyewall during the deepening stage, a pronounced eyewall replacement with double eyewalls before evolving to a near-concentric eyewall during its maintaining phase, and several interesting structural changes in between. Although a 5-day simulation of the same case has already been performed by Rogers et al. (2003), they used National Centers for Environmental Prediction (NCEP) analysis without bogussing a vortex in the model initial conditions, the nudged mass and wind fields in the outer mesh during the first 72-h integration, a simple ice microphysics scheme, and fixed sea surface temperatures (SSTs) in time. As a result, the initial storm was 12–15 hPa weaker, but the mature storm was 30 hPa deeper than the observed. Thus, the hurricane intensity and intensity changes as well as inner-core structures could not be realistically studied with their simulation.

The next section provides an overview of the storm development. Section 3 describes the basic features of MM5 used for this study. Section 4 presents the simulation results as verified against detailed observations. Sections 5 and 6 discuss the impact of vertical wind shear on the hurricane intensity changes and cloud asymmetries, respectively. Section 7 shows the evolution of eyewall replacement with double-eyewall structures. A summary and concluding remarks are given in the final section.

## 2. Overview of Hurricane Bonnie

Originating over the west coast of Africa, Bonnie had a long life span of development. It exhibited a large cyclonic circulation at the lower and middle levels over Dakar, Senegal, on 14 August 1998. By 1200 UTC 19 August, its central pressure fell to 1009 hPa and reached tropical depression stage. After 24 h, the pre-Bonnie depression was upgraded to a tropical storm, with the minimum pressure of 1007 hPa and maximum surface wind of  $17.5 \text{ m s}^{-1}$ . Bonnie moved west-northwestward under the steering flow associated with the Bermuda high (see Figs. 1 and 2). It became a category 1 hurricane at 0600 UTC 22 August, with the minimum center pressure of 989 hPa after it entered into a favorable upper-level anticyclonic circulation. Thereafter, Bonnie deepened significantly, at a rate of  $0.9 \text{ hPa h}^{-1}$ , and reached its minimum pressure of 954 hPa at 0000 UTC 24 August (see Fig. 3). Although a near-concentric eyewall could be seen from the National Oceanic and Atmospheric Administration’s (NOAA’s) WP-3D aircraft

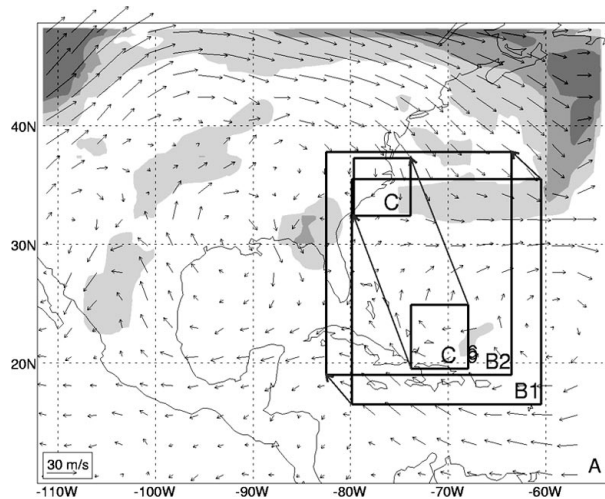


FIG. 1. The nested model meshes, with horizontal resolutions of 36, 12, and 4 km for domains A, B, and C, respectively, superposed with the 200-hPa wind vectors and potential vorticity (shaded at every 1 PVU) at 0000 UTC 22 Aug 1998.

composite radar image at 2100 UTC 21 August (not shown), the convective cloud structure (see Fig. 7a) was very asymmetric, with most of the reflectivity on the northeast side of the eyewall during most of the time from 22 to 25 August.

After reaching its minimum central pressure, Bonnie weakened to 960 hPa by 0600 UTC 24 August (see Fig. 3). Then, Bonnie maintained its intensity during the next 3 days until it made landfall near Wilmington, North Carolina, at 0400 UTC 27 August, with the minimum pressure of 964 hPa. Radar reflectivity patterns indicate that the storm's asymmetric structures remained until the beginning of 25 August (not shown), and the storm structures are more axisymmetric during the next 2 days prior to landfall (see Fig. 7c). See the preliminary report by Pasch et al. (2001) for a more detailed description of the evolution of Bonnie.

To summarize, Bonnie exhibited two distinct characteristics during its life span. The first one is the evolution of storm intensity showing a significant deepening for a 2-day period after reaching category 1 on 22 August 1998, followed by a near steady state over the open ocean during the next 3 days (i.e., 24–27 August). The second distinct characteristic is the evolution of precipitation in the eyewall, that is, from a concentric eyewall to a partial and then near-concentric eyewall during 21–27 August. Some of the features were well sampled by a field campaign carried out by Hurricanes at Landfall/Third Convection and Moisture Experiment (HAL/CA-MEX3) program. Thus, Bonnie appears to be an interesting case to study the physical and dynamical processes leading to the hurricane intensity change and asymmetric eyewall structures.

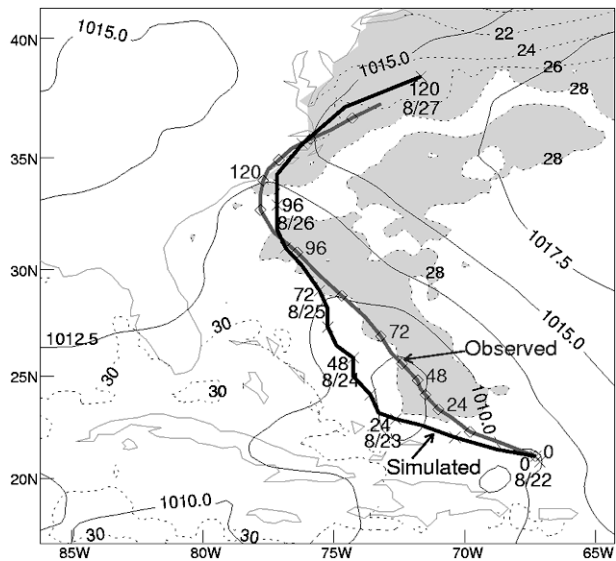


FIG. 2. Tracks (6 h) of Bonnie from the best analyses (light thick lines) and the model simulation (dark thick lines), superposed with the 5-day (0000 UTC 22–0000 UTC 27 Aug) averaged sea level pressure (solid lines) and SST (dotted, with its value of less than 28°C shaded).

### 3. Model description

In this study, Hurricane Bonnie (1998) is explicitly simulated using the latest version (V3.4) of the PSU–NCAR nonhydrostatic, two-way interactive, movable, triply nested grid model (i.e., MM5; Dudhia 1993; Grell et al. 1995) with the finest grid length of 4 km. The model physics used include the Tao–Simpson (1993) cloud microphysics scheme, the Kain–Fritsch (1993) convective parameterization scheme, the Blackadar PBL scheme (Zhang and Anthes 1982), and a cloud–radiation interaction scheme that are all similar to those used by Liu et al. (1997). Although no convective parameteri-

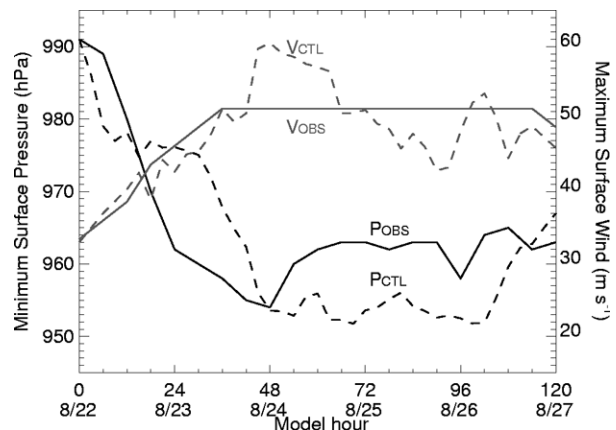


FIG. 3. Time series (6 h) of the minimum central pressures ( $P$  in hPa) and the maximum surface winds ( $V$  in  $\text{m s}^{-1}$ ) from the best analysis (solid;  $P_{\text{OBS}}$  and  $V_{\text{OBS}}$ ) and the model simulation (dashed;  $P_{\text{CTL}}$  and  $V_{\text{CTL}}$ ).

TABLE 1. The model design.

Domain	Mesh A	Mesh B	Mesh C
Grid points (x,y)	180 × 142	184 × 202	163 × 163
Grid size (km)	36	12	4
Time step(s)	90	30	10
Integration hours	0–120	B1: 0–10; B2: 10–120	12–120
Explicit moisture	Tao–Simpson (1993)	Tao–Simpson (1993)	Tao–Simpson (1993)
Cumulus scheme	Kain–Fritsch (1993)	Kain–Fritsch (1993)	No
PBL parameterization	Blackadar (1982)	Blackadar (1982)	Blackadar (1982)

zation is applied over the finest mesh, a shallow convective scheme is used. There are 24  $\sigma$  levels or 23 half- $\sigma$  layers in the vertical, which is the same as that used by Liu et al. (1997). Table 1 describes the model design, and Fig. 1 shows the model domains.

A 5-day simulation is performed, covering the initial deepening, steady variation, and landfalling stages of the storm, and it is initialized at 0000 UTC 22 August with the two outmost meshes. After 10 h into the integration, the second mesh is moved once northwestward from B1 to B2 to cover more realistically the hurricane-scale flows with a limited grid area (see Fig. 1). The third mesh C is activated at 12 h into the integration, and it is automatically moved with the storm. In this automatic mesh-movable scheme, the center of mesh C is moved to coincide with the storm center every 6 h, with the latter determined by the maximum column-averaged relative vorticity. Data in the leading portion of the moving finer mesh is always interpolated from its mother mesh (see Liu et al. 1997).

The model initial conditions and lateral boundary conditions are obtained from the NCEP  $2.5^\circ \times 2.5^\circ$  global analysis, which is then enhanced by rawinsondes and surface observations. Because the NCEP analysis contains a vortex with a central pressure of 12 hPa weaker than the observed, an observation-based vortex is incorporated into the model initial conditions. In this initial vortex, the three-dimensional temperature and moisture fields are retrieved from the Advanced Microwave Sensing Unit-A (AMSU-A) measurements; the asymmetric vortex flows are obtained by solving the nonlinear balance and omega equations, using the NCEP analysis as the lateral boundary conditions; and some surface parameters are specified from the HAL/CAMEX3 observations (see Zhu et al. 2002). Since this is a 5-day simulation, the oceanic feedback becomes an important factor influencing the intensity of the storm. For this reason, the SST is updated daily using the Tropical Rainfall Measuring Mission (TRMM) Microwave Imager (TMI) level 1 standard product at  $0.25^\circ \times 0.25^\circ$  latitude–longitude resolution (Chelton et al. 2000). Although the TMI SST can be measured underneath clouds, there are still some missing data near the storm center because of the contamination by heavy rainfall. They are filled by a 3-day running mean of SST at each grid point where the data were missed, using the data up to the current model time. The 5-day averaged SST

distribution is given in Fig. 2, which shows more than  $2^\circ\text{C}$  cooling along and to the north of Bonnie's track. According to our sensitivity test, to be shown in a forthcoming paper, and the coupled ocean–atmosphere model simulations of Hong et al. (2000), this SST cooling could account for about 20-hPa central pressure changes in simulations with or without the SST feedback.

#### 4. Model verification

In this section, we verify the simulation results against various observations from the HAL/CAMEX3 program to see how well the model could reproduce the observed hurricane intensity and structural changes. First, the simulated track is compared to the observed in Fig. 2, which shows similar paths in the first 12 h. Then, the storm changed its tracking direction from west-northwest to northwest, whereas the simulated one keeps moving west-northwestward. The simulated storm does not begin to move northwestward until after 24 h. The faster displacement is also simulated during the 12–48-h period. As a result, the simulated track deviates from the observed by about 200 km at 24 h. This error, carried over until landfall, is likely caused by the model's failure to reproduce the weakening of the Bermuda high. According to Pasch et al. (2001), the ridge to the north of Bonnie weakened temporarily, leading to the collapse of the steering currents during the first 48 h. As the storm broke through the subtropical high, it drifted northward at a slower speed. By comparison, the simulated storm moves closer to the best track after 48 h, but still with a distance error of 250 km, and it also recurves somewhat earlier than the observed at 84 h. Thus, the simulated landfall occurs to the northeast of the observed by about 150 km and 20 h earlier. This error is introduced during the first 12–48-h period, as mentioned earlier, when Bonnie is in its deepening phase. After landfall, the simulated storm turns northeastward and accelerates. Although the track follows closely the observed, the simulated displacement is unrealistically too fast. Therefore, the following presentation will focus more on the first 108-h simulation prior to landfall. It should be mentioned that almost all of the then-operational model forecasts, initialized with the NCEP analysis on 22 August, did not indicate the likelihood of landfall of the storm (Avila 1998). This also appears to be one of the reasons why a dynamical nudg-



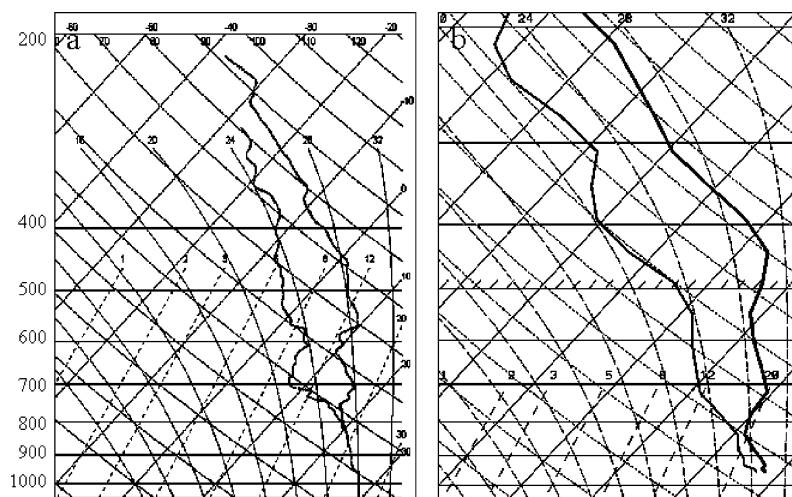


FIG. 4. (a) Dropsonde released by DC-8 aircraft in the eye of Hurricane Bonnie at 2126 UTC 23 Aug (see Fig. 7a for its location) and (b) a simulated sounding at the eye center at 2130 UTC 23 Aug 1998 (see Fig. 7b later for its location).

ing algorithm was used in Rogers et al. (2003) in order to obtain a reasonable simulation of the storm track. Our success in reproducing the hurricane track could be attributed to the use of more complete observations, such as the AMSU-based hurricane initial vortex and TMI SST.

Figure 3 compares the simulated hurricane intensity to the observed. They are in general agreement but differ in details during the 5-day period. Initially, the modeled storm ( $P_{CTL}$ ) deepens more rapidly than the observed ( $P_{OBS}$ ), indicating the absence of the model spinup problem. This appears to be partially attributable to the specification of relatively high moisture content in the initial hurricane vortex. However, the model storm experiences a slow deepening period from 12 to 30 h. This is likely caused by the presence of a too dry environment that fails to feed the needed energy in the PBL inflow for the continued deepening, since the initial moisture field outside of the hurricane vortex was not modified in the model initial conditions (see Zhu et al. 2002). A deepening rate, similar to the observed, does not occur until the 30-h simulation, when the model storm begins to receive comparable energy supply through the air–sea interaction processes. The simulated storm deepens and reaches the minimum central pressure of 954 hPa as did the observed at 48 h. It maintains its intensity with weak oscillations afterward, whereas the observed experienced a 6-h weakening period from 48 to 54 h and maintained its intensity between 958 and 964 hPa during the remaining period. On average, the two storms differ 6–8 hPa during the maintenance stage. Part of this difference could clearly be attributed to the fact that the simulated storm moves to the south of the best track in the first 3 days, where local SST is about 2°C warmer than that to its north (see Fig. 2). Nevertheless, the two distinct development stages of rapid deepening and slow

maintenance are considered reasonably reproduced. Of interest is that an eyewall replacement scenario appears from 72 to 96 h in both the observed and the modeled storms, albeit with different periods. During this period, the central pressure fills 2–4 hPa, followed by a deepening of similar magnitude; its causes will be explored in section 7.

The simulated maximum surface winds ( $V_{CTL}$ ) also compare favorably to the observed ( $V_{OBS}$ ). The simulated  $V_{CTL}$  keeps increasing to about 60 m s<sup>-1</sup> until 48 h, at which time the sea level pressure is a local minimum and oscillates at that intensity during the maintaining stage (Fig. 3). However, such an oscillation is not evident in the observations; even the sea level pressure field exhibits significant changes, for example, during the periods of 30–54 h and 90–102 h. In this regard, the simulated maximum surface wind and minimum sea level pressure are more dynamically consistent. Again, Bonnie's two distinct development stages could be clearly seen from both the simulated and observed wind fields.

Figures 4 and 5 compare the two simulated soundings to the observed that are taken near the eye center and in a major rainband located at about 100 km to the northeast of the center, respectively. Because of the tracking errors, the sounding comparisons are made in accordance with their relative locations to the hurricane center. A dropsonde taken in the eye (Fig. 4) shows a saturated layer below 800 hPa with a deep dry layer aloft and two inversion layers: one in the 750–700-hPa layer and the other in the 620–570-hPa layer. This sounding is a typical one in the eye (Franklin et al. 1988), and it appears to be generated by high- $\theta_e$  (i.e., equivalent potential temperature) fluxes from the underlying warm ocean and dynamically induced subsidence aloft (Zhang et al. 2000). The simulated eye sounding is about 1°–

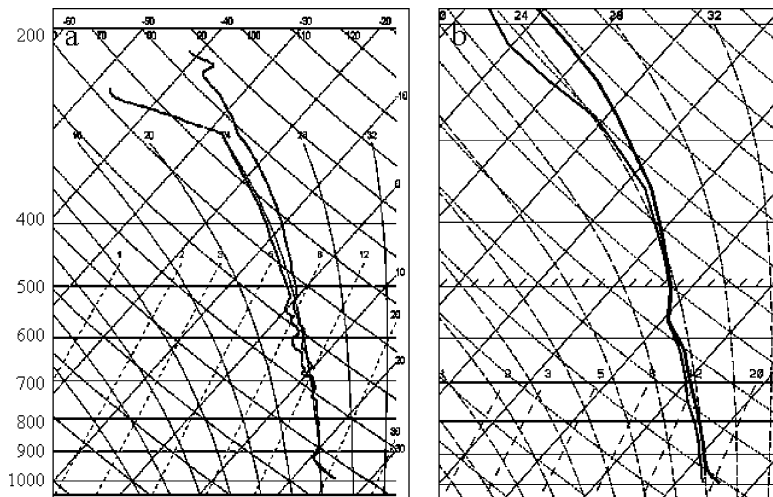


FIG. 5. As in Fig. 4, but in (a) the observed major rainband at 2119 UTC 23 Aug and (b) the simulated rainband at 2130 UTC 23 Aug 1998; they are located about 100 km to the northeast of the center (see Fig. 7 later for their approximate locations).

2°C warmer throughout and dryer above 500 hPa than the observed. Nevertheless, the model sounding also exhibits a relatively moist boundary layer below 820 hPa, albeit unsaturated, with a dry air aloft and two inversion layers above. While occurring at approximately similar altitudes, the simulated characteristic layers are deeper than the observed, likely because of the relatively coarse resolution in the model vertical layers.

Both the dropsonde and the simulated sounding taken in the rainbands, where heavy precipitation occurs, dis-

play a near-saturated thermal structure up to 500 hPa (Fig. 5) and follow closely the 24°C pseudoadiabatic contour. There is a weak cooling layer around the 0°C level (or 550 hPa) in both the simulation and observation, in association with the melting of graupel and snow. Below 900 hPa, the dropsonde shows a dry adiabatic but saturated lapse rate, which is likely caused by some instrument errors.

Figure 6 compares the simulated thermal and horizontal wind fields in the west–east vertical cross sections

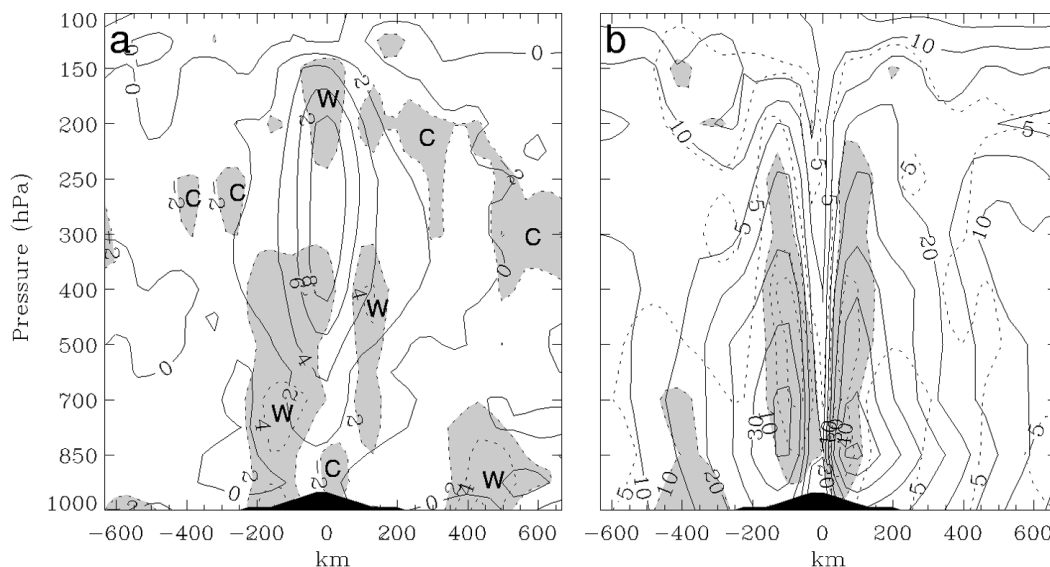


FIG. 6. South–north vertical cross sections through the center for (a) the temperature anomalies (solid) at intervals of 2°C from the 84-h simulation valid at 1200 UTC 25 Aug and the differences (dashed, with greater than  $\pm 2^\circ\text{C}$  shaded) from the AMSU-A retrieved temperature (i.e.,  $T_{\text{MM5}} - T_{\text{AMSU}}$ ) at 0000 UTC 26 Aug and (b) the corresponding tangential winds (solid) at intervals of  $5 \text{ m s}^{-1}$  and the differences (dashed, with greater than  $\pm 10 \text{ m s}^{-1}$  shaded) from the AMSU retrieved (i.e.,  $V_{\text{MM5}} - V_{\text{AMSU}}$ ). Letters “W” and “C” in (a) denote the warm and cold biases, respectively, in the modeled field.

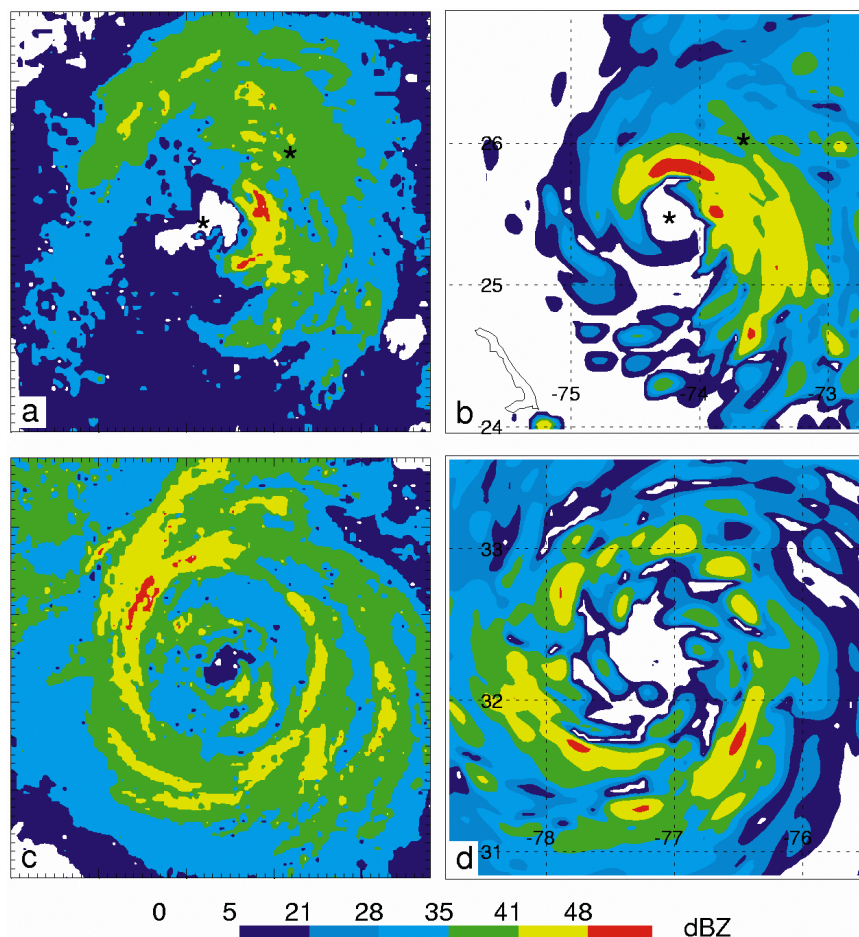


FIG. 7. Comparison of the observed radar reflectivity from NOAA's WP-3D reconnaissance aircraft at (a) 2200 UTC 24 Aug at  $z = 4572$  m and (c) 1240 UTC 26 Aug at  $z = 3518$  m to (b) the 51-h simulated ending 0300 UTC 24 Aug near 500 hPa and (d) the 93-h simulated ending 2100 UTC 25 Aug near 550 hPa. The symbol \* in (a) and (b) shows the locations of the soundings shown in Figs. 4 and 5; (a)–(d) have the same color scale and the same domain size of  $360 \text{ km} \times 360 \text{ km}$ .

to the AMSU retrieved [see Zhu et al. (2002) for a detailed description of the retrieval algorithm and errors]. Note that the retrieved data at 0000 UTC 26 August are compared to the simulated at 84 h because of (a) the availability of AMSU data for such a comparison and (b) the closest locations of the two storms (see Fig. 2). Major differences in temperature anomalies occur below 500 hPa in the eyewall ( $R = \pm 100 \text{ km}$ ) and below 850 hPa in rainbands ( $R = 500 \text{ km}$ ), where the simulated temperature is about  $4^\circ\text{C}$  warmer than the retrieved. These differences are acceptable because the AMSU measurements tend to produce cold biases in the presence of heavy precipitation [see Zhu et al. (2002) for a related discussion]. However, the simulated warmer temperatures above 250 hPa in the eye and colder temperatures in the layer of 200–400 hPa over the outer regions indicate that the simulated warm core is deeper and narrower than the retrieved partly because of different resolutions and partly because of different inten-

sities. Nonetheless, the stronger warm core is consistent with the development of a more intense storm in the model (see Fig. 3). Otherwise, the simulated temperature anomalies are in reasonable agreement with the retrieved in most areas, including the height of the warm core [cf. Fig. 6a herein and Fig. 4b in Zhu et al. (2002)].

Because the modeled storm has a smaller size but stronger intensity, the radius of maximum wind (RMW) is about 10 km smaller and the wind speeds are up to  $20 \text{ m s}^{-1}$  stronger than the retrieved. However, the model reproduces quite well an asymmetric wind speed structure with stronger (weaker) flow to the north (south), similar to the AMSU retrieved [cf. Fig. 10a in Zhu et al. (2002) and Fig. 6b herein].

Figures 7a–d compare the horizontal distribution of simulated radar reflectivity at 51 and 93 h to the observed at 2200 UTC 24 and 1240 UTC 26 August, respectively. Note that because of the 200-km distance (or equivalently, 15-h time) error after the 48-h inte-

gration, it is more meaningful to compare the simulated to the observed cloud asymmetries based on their closest locations (e.g., as given in Fig. 7), particularly when considering the impact of environmental flow. It is evident from Figs. 7a,b that both the simulated and observed precipitating clouds are highly asymmetric, with deep convection (convective and stratiform clouds) in the northeast quadrant of the eyewall (outer regions). The observed and simulated eyewall sizes are about 50 km in radius. Of particular interest is that little convection occurs in the southwest quadrant of the storms. This partial eyewall structure was clearly visible from NOAA's WP-3D radar reflectivity and TRMM rain-rate observations as early as 0000 UTC 22 August (i.e., the model initial time) and until 1200 UTC 25 August (not shown). When Bonnie moved close to the east coast of the United States, the observed reflectivity became more axisymmetric and exhibited a near-concentric eyewall with a radius of approximately 100 km and a weak inner rainband at a radius of about 30 km (Fig. 7c)—an indication of the eyewall replacement. The simulated reflectivity compares favorably to the observed in terms of the axisymmetric cloud distribution and the eyewall size during this stage (Fig. 7d).

Heymsfield et al. (2001) provided a comprehensive overview of the Doppler radar observations taken in Bonnie by ER-2 and DC-8 aircraft. Thus, it would be of interest to examine how well the model could reproduce the radar-observed vertical structures. The observed reflectivity shows the development of deep convection in the eastern portion of the eyewall with an echo intensity as strong as 60 dBZ in the 4–6-km layer and precipitating clouds as deep as 14 km (Fig. 8). Like the horizontal reflectivity pattern, deep convection and clouds also developed in the outer rainbands (cf. Figs. 7a and 8a), which were hardly separable from those in the eyewall except for their different intensities. In contrast, there were some less organized shallow rainbands on the west and upper-level clouds near the “eye” center (i.e.,  $R = 0$  km). It is evident that the model reproduces many of the observed vertical structures, including the sloping eyewall and its radial size, the outer rainbands and inseparable cloud distribution from the eastern eyewall, and the shallow clouds to the west. Although little upper-level clouds are present near the eye center in this cross section, upward motion does develop in the same eye layers as the observed clouds (cf. Figs. 8a,b). Furthermore, the simulated RMW is located about 10 km outside of the most intense outward-titled updrafts in the eastern eyewall, but the local RMW in the western “eyewall” occurs in the weak vertical motion zone and tilts slightly inward. Of interest is that the simulated hurricane center, defined by its minimum pressure, also exhibits an eastward tilt with height at a slope of 2:5. This tilt is clearly caused by the tremendous latent heating in the eastern eyewall and by the advection of the westerly sheared flow as indicated by the in-plane flow vectors. These features will be the subject of section 6.

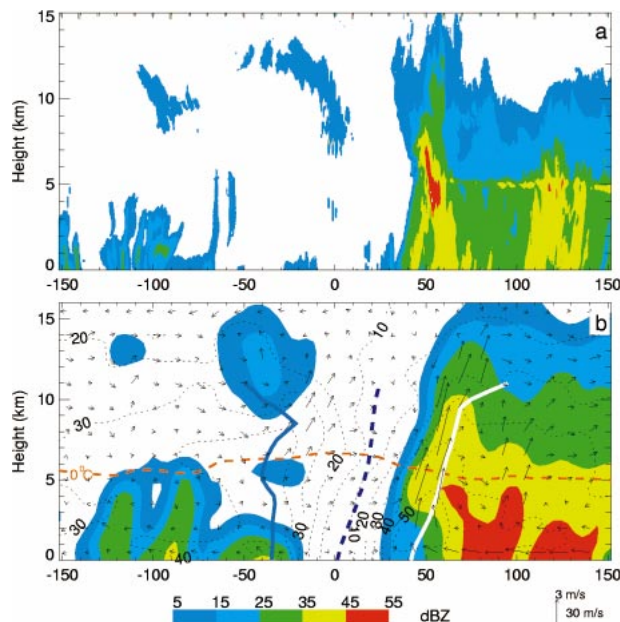


FIG. 8. West-east vertical cross sections of radar reflectivity through the center from (a) NASA's ER-2 aircraft Doppler radar during the 1950–2100 UTC 23 Aug flight leg and (b) the 45-h simulation valid at 2100 UTC 23 Aug 1998, superposed with in-plane flow vectors and the vertical axes of RMW (thick solid lines) and the minimum pressures (thick dashed lines). Horizontal wind speeds (dotted lines) are shown at intervals of  $10 \text{ m s}^{-1}$ . The melting level (i.e.,  $0^\circ\text{C}$ ) is also plotted.

Note the presence of a bright band in the observed reflectivity at  $z = 5$  km that is an indicator of the height of the melting layer. The bright band is formed largely because of the modification of the attenuation and backscattering by the melting of ice particles, and it does not mean that the rain rate is increased in this narrow band (Sauvageot 1992). Because the  $Z$ – $R$  relationships used to derive the modeled radar reflectivity (Liu et al. 1997) do not consider these effects, Fig. 8b does not show a bright band. However, the height of the simulated  $0^\circ\text{C}$  isotherm is consistent with that of the observed bright band.

In summary, the model reproduces reasonably well the track, intensity, inner-core structures, and evolution of Bonnie as verified against various field observations. Despite some timing and location errors, the simulation results can be utilized to study the processes leading to the development of a partial eyewall, its replacement by a near-concentric eyewall, various intensity change scenarios, the vertical tilt of the hurricane circulation, the eye expansion, and the other inner-core features.

## 5. Intensity changes and vertical shear

Several observational and idealized modeling studies have shown the important influences of vertical wind shear on hurricane intensity changes (DeMaria 1996; Bracken and Bosart 2000; Frank and Ritchie 2001;



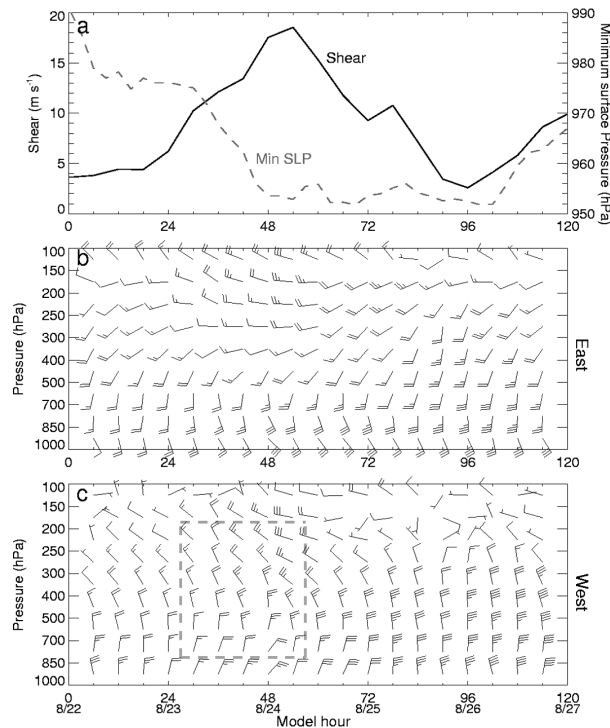


FIG. 9. (a) Time series of the area-averaged (i.e.,  $1000 \text{ km} \times 1000 \text{ km}$ ; see boxes in Figs. 10 and 11) magnitude of simulated vertical shear vectors between 200 and 850 hPa and the simulated pressure–time cross sections of the averaged horizontal winds over the (b) eastern and (c) western half portions of the storm (i.e.,  $500 \text{ km} \times 1000 \text{ km}$ ; see boxes in Figs. 11 and 12). A full barb in  $5 \text{ m s}^{-1}$ . The dashed box in (c) shows the distribution of positive vertical shears. For the sake of comparison, the simulated 6-h minimum central pressures (dashed), shown in Fig. 3, are also given in (a).

Black et al. 2002). Thus, here we examine to what extent Bonnie's intensity changes, given in Fig. 3, could be explained by the vertical wind shear. For this purpose, we show first in Fig. 9a the time series of the area-averaged ( $1000 \text{ km} \times 1000 \text{ km}$ ) vertical shears between 200 and 850 hPa; these two levels were typically used to estimate vertical shears in previous studies. It is evident that the vertical shears increase in magnitude with time and reach a peak value of  $19 \text{ m s}^{-1}$  at 54 h. Subsequently, the shear magnitude drops rapidly to about  $5 \text{ m s}^{-1}$  at 84 h and maintains its value in the remaining hours prior to landfall. Of importance to note is that *the storm intensifies simultaneously with the vertical shear during the first 2 days* (see Fig. 9a). This appears to contradict with the previous findings that the vertical shear tends to produce negative impact on the intensification of tropical cyclones (Gray 1968; Anthes 1982; DeMaria 1996). A common explanation for this effect is “ventilation” of the hurricane warm core. A recent composite analysis of 139 storms over the Atlantic basin by Bracken and Bosart (2000) showed that the vertical shear between 200 and 900 hPa for developing tropical cyclones is about  $10 \text{ m s}^{-1}$ . Black et al. (2002) found that Hurricane Jimena (1991) was able to maintain cat-

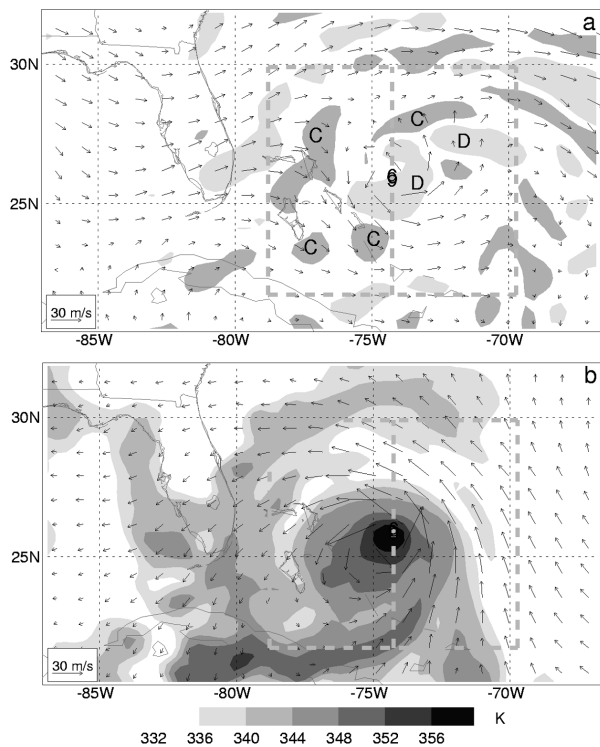


FIG. 10. Horizontal distribution of flow vectors at (a) 200 hPa with divergence (“D”) and convergence (“C”) shaded ( $2.5 \times 10^{-5} \text{ s}^{-1}$ ) and (b) 850 hPa with equivalent potential temperature  $\theta_e$  (shaded at intervals of 4 K); they are from the 48-h simulation valid at 0000 UTC 24 Aug 1998. Hurricane symbol denotes the location of the minimum surface pressure. The thick dashed interior frame represents the area used for averaging the flow fields shown in Fig. 9.

egory 4 intensity in  $13\text{--}20 \text{ m s}^{-1}$  shear, and Hurricane Olivia (1994) strengthened markedly in  $8 \text{ m s}^{-1}$  vertical shear. Elsberry and Jeffries (1996) found that Tropical Cyclones Omar (1992) and Steve (1993) could form and intensify with vertical wind shears exceeding  $12.5 \text{ m s}^{-1}$ . Apparently, the relationship between the intensity change of tropical cyclones and vertical wind shear is more complex than the earlier “ventilation” hypothesis. Further studies are clearly needed to help understand the impact of environmental flow on hurricane intensity and intensity changes.

It is obvious that hurricane intensity depends essentially on the magnitude and distribution of latent heat release in the eyewall. The vertical wind shear affects hurricane intensity through the development of deep convection in the eyewall. An examination of the vertical distribution of horizontal winds reveals that the area-averaged vertical shears shown in Fig. 9a are made up mostly by winds in two different air masses: a south to southeasterly low-level jet to the east with a negative vertical (speed) shear above the PBL (Figs. 9b and 10b) and a strong northwesterly upper-level flow to the west of the storm with a positive vertical (speed) shear (at least from 30 to 54 h) (Figs. 9c and 10a). It is well known that an increase and a decrease in horizontal

winds above the PBL have different implications for the development of organized convective systems in mid-latitudes. In the present case, the former (inflow) appears to play an important role in transporting tropical high- $\theta_e$  air (Fig. 10b) and cyclonic angular momentum into the system, accounting for the development of deep convection in the eastern half of the eyewall and the deepening of Bonnie. Other favorable conditions that may contribute to its rapid deepening include the presence of (a) high SST (i.e.,  $>28.5^\circ\text{C}$ ) along the track until 42 h (see Fig. 2) and (b) persistent upper-level divergent, anticyclonic outflows over the storm (see Figs. 1 and 10a).

In contrast, the increasing northwesterly flow with height, as shown in Fig. 9c, has detrimental impact on the intensification of Bonnie. This flow is associated with an upper-level short-wave trough that deepens in the middle of the two near-stationary larger-scale anticyclones (cf. Figs. 10a and 1) as a result of the transport of a potential vorticity anomaly from the northern latitudes (not shown). This trough interacts with the hurricane's outflows, leading to a narrow annulus of convergence in the northern semicircle (Fig. 10a). It is this upper-level convergence zone—particularly the one upstream, as indicated by “C” in Fig. 10a—that causes the descending inflow into the western portion of the “eyewall” (cf. Figs. 10a and 8b). This descending inflow tends to suppress the local cloud development and force the hurricane's warm core to tilt toward the active convective region in the eastern semicircle (Fig. 8b). Evidently, the above-mentioned favorable conditions must overcompensate the negative effect of the northwesterly shear in order for the storm to intensify significantly in the first 2 days.

The scenarios described above are to a certain extent similar to the idealized sensitivity simulations of Frank and Ritchie (2001), who showed a time lag between when a vertical shear is introduced and when the storm stops its deepening. This time lag varies from 3 h to as long as 36 h, as the vertical shear increases from 5 to  $15\text{ m s}^{-1}$ . Based on the above discussion, we may see that the vertical shear introduced on the upshear side plays a role in weakening the storm, whereas the eyewall convection on the downshear side tends to intensify it. The relative magnitudes between the positive and negative forcings provide a good explanation of the time lags among the different sheared cases being tested. Thus, our result suggests that it is necessary to examine various parameters that determine the magnitude and distribution of latent heat release in the eyewall, and the previous approach of using the vertical shear to estimate hurricane intensity change does not seem to be applicable to all hurricane cases.

After 60 h, Bonnie moves northeastward farther away from the stationary anticyclone over the Gulf of Mexico so that the influence of upper-level flow diminishes (Fig. 11a). As a result, the eyewall undergoes a period of rapid adjustment (see Fig. 14) with double-eyewall

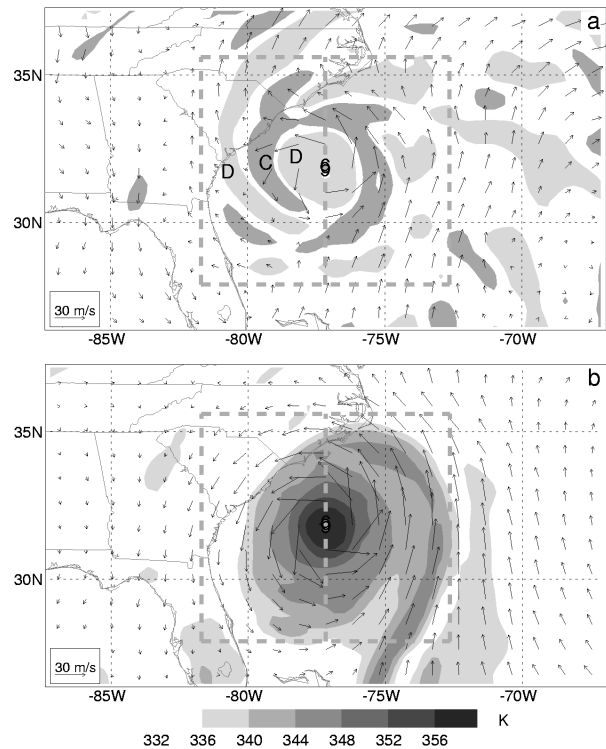


FIG. 11. As in Fig. 10, but from the 90-h simulation valid at 1800 UTC 25 Aug 1998.

structures, to be shown in section 7, that ends up with more axisymmetric distributions of clouds and precipitation and storm-scale anticyclonic outflow aloft (Figs. 9b,c and 11a). However, Bonnie has now moved to a colder ocean surface with more negative influences of continental (dry) air mass (and later surface friction). Moreover, the eyewall has expanded in radius with relatively weak convection within. Thus, the storm is unable to intensify prior to landfall (i.e., from 48–102 h; see Fig. 3).

## 6. Inner-core structures and vertical shear

In this section, we examine the influence of vertical wind shear on the development of the partial eyewall and other related inner-core structures. Figure 12 presents a time–azimuth cross section of the simulated radar reflectivity along the updraft core at  $z = 5\text{ km}$ . The partial cloudy eyewall can be clearly seen as a dominant wavenumber-1 asymmetry during the first 84-h integration. Most of the clouds and intense precipitation develop in the northeast quadrant, whereas the southwest semicircle is often cloud-free prior to 72 h. Subsequently, precipitating clouds spread quickly to form a near-concentric eyewall. Similar features could also be seen from the observations of NOAA's WP-3D radar and TRMM surface rainfall rates (not shown).

The cloud asymmetry shown in Fig. 12 could be well related to the vertical wind shear. In fact, previous mod-

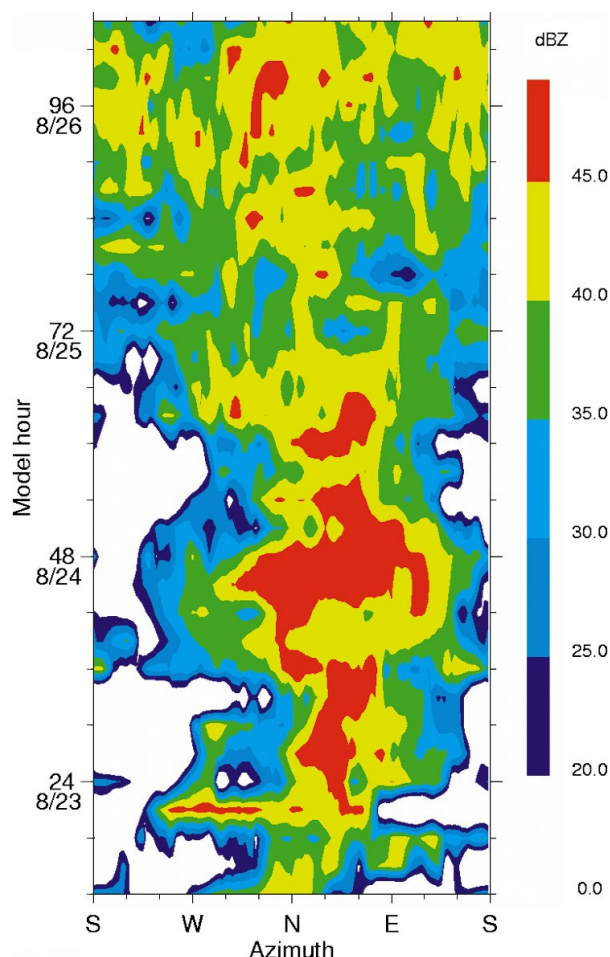


FIG. 12. The time-azimuth cross section of the simulated radar reflectivity along the updraft core at  $z = 5$  km.

eling studies (e.g., Frank and Ritchie 2001) showed that tropical cyclones tend to develop wavenumber-1 asymmetries when the mean vertical shear is greater than  $5 \text{ m s}^{-1}$ . In the present case, the wavenumber-1 asymmetries in radar reflectivity occur in the first 72 h in coincidence with the duration of vertical shear being greater than  $5 \text{ m s}^{-1}$  (cf. Figs. 9a and 12). Furthermore, Fig. 13 shows that the maximum upward motion and reflectivity in the eyewall are mostly located at the downshear-left side (i.e., the northeast quadrant) during the first 72 h. This downshear-left pattern is consistent with the general area of continued clouds and precipitation development (cf. Figs. 12 and 13), and it is similar to that in the previous observations (e.g., Willoughby et al. 1984; Marks et al. 1992; Franklin et al. 1993; Black et al. 2002) and idealized simulations (e.g., Bender 1997; Frank and Ritchie 1999; Ritchie and Elsberry 2001).

To help gain insight into the influence of the upper-level westerly flow on the eyewall development, Fig. 14 shows a time and west-east cross section of the  $u$  velocity at  $z = 11$  km and the upward motion at  $z = 5$

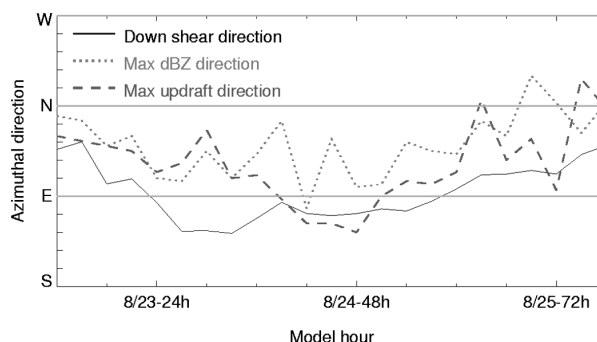


FIG. 13. Time series of the azimuthal distributions of the area-averaged vertical wind shears (solid), the maximum upward motion (dashed), and the maximum radar reflectivity (dotted).

km. The upper-level flow during the first 12 h is near symmetric, with an anticyclonic outflow within  $R = 100$  km. Subsequently, the upper-level westerly component intensifies, reaching a peak of  $19.0 \text{ m s}^{-1}$  by 54 h, and dominates the western semicircle of Bonnie. It even extends to the storm's central core from 42 to 72 h, clearly assisting the ventilation of warm air in the eye

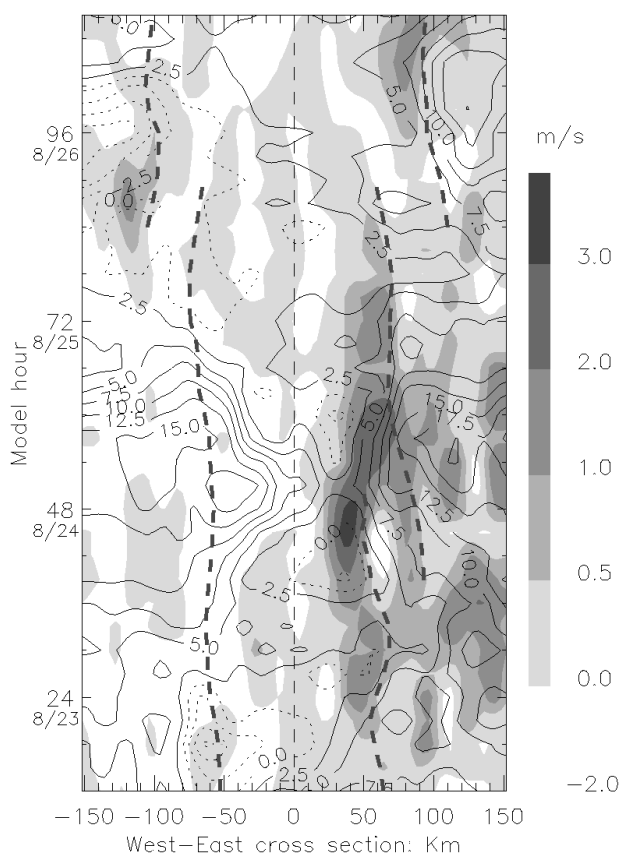


FIG. 14. Time and west-east cross section, through the simulated hurricane center, of the  $u$  component (every  $2.5 \text{ m s}^{-1}$ ) at  $z = 11$  km, the upward motion (shaded), and RMW (thick dashed) at  $z = 5$  km. Solid and dotted lines denote the westerly and easterly  $u$  components, respectively.



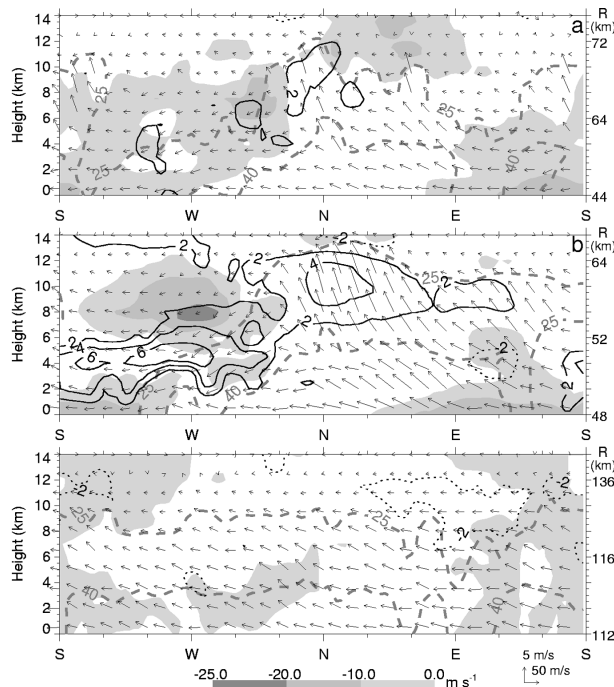


FIG. 15. Height–azimuth cross sections of temperature deviations (positive/solid, negative/dotted), radial inflow (shaded), reflectivity (thick dashed), and in-plane flow vectors that are taken in a vertically slantwise surface (see the changes in radius size with height on the right) through the maximum reflectivities in the eyewall from (a) 36-, (b) 48-, and (c) 90-h simulations. They are valid at 1500 UTC 23, 0000 UTC 24, and 2100 UTC 25 Aug 1998, respectively.

(cf. Figs. 14 and 8b). The cross-sectional mass convergence (divergence) corresponds well to the local descent (ascent) in the midtroposphere that suppresses (promotes) cloud development in the western (eastern) eyewall. Few organized updrafts appear on the west in the first 72 h. Of interest is that little changes in the RMW (at  $z = 5$  km) occur in the first 48 h despite the storm's rapid deepening. Subsequently, the RMW in the east semicircle is replaced by a secondary RMW associated with an intense outer rainband that develops at 42 h into the simulation. Of more significance is the development of two RMWs (and eyewall) just prior to the formation of a near-concentric eyewall (i.e., from 84 to 90 h; see Figs. 12 and 14). They are evidence of the eyewall replacements and will be discussed in section 7.

Figure 15 shows how the eyewall interacts with the environmental flows in generating the cloud asymmetries. At 36 h, a deep low-level moist flow transports the high- $\theta_e$  air from the southeast quadrant to facilitate the development of updrafts in the eyewall (Fig. 15a). The ascending airstreams tilt cyclonically upward from the southeast to northeast quadrant, as being advected by strong swirling flows, and intensify as a result of latent heat release. Because intense updrafts in the eyewall are typically supergradient (Zhang et al. 2001), radial outflows overwhelm the north semicircle. The warm deviations or anomalies in the upper outflow layer

(i.e., centered at  $z = 10$  km) result from the outward advection of the warm eye air, according to Zhang et al. (2002). (All deviations are obtained by subtracting their azimuthally and radially averaged values at individual heights.) On the other hand, the upper-level westerly flow begins to enter the eyewall with a deeper and stronger inflow in the northwest. Because the environmental air is cold and dry, downdrafts are initiated in the inflow (cold advection) region, with the significant enhancement from evaporative cooling. The dry descending airstreams also tilt cyclonically, but downward, thereby suppressing the developments of clouds and precipitation in a large portion of the western "eyewall," as indicated by the downward-tilted reflectivity contours. In the absence of clouds and precipitation, dry descent causes the adiabatic warming and drying, thus generating warm anomalies in the eyewall (see Figs. 15 and 18b), despite the presence of cold advection in inflow regions (see Zhang et al. 2002).

During the maturing stage (i.e., at 48 h), the partial eyewall becomes more pronounced and the vertical wind shear nearly reaches its peak value (Fig. 9a). The increased shearing effect is evidenced by the intensifying west to northwesterly inflow, with the center shifting from the northwest to the west (cf. Figs. 15a,b). Thus, more significant descending flows appear in the western eyewall, causing pronounced adiabatic warming (and drying). Warm anomalies of greater than  $6^\circ\text{C}$  with little clouds and precipitation can be found in the lower portion of the eyewall over the southwest quadrant. In contrast, well-organized, intense updrafts dominate the eastern semicircle at this stage, leading to strong supergradient outflows, particularly in the upper outflow layer where significant warm anomalies are present. Note that *this wavenumber -1 cloud asymmetric pattern moves downward with time because of the presence of the upper-level descending inflow*.

A west–east vertical cross section taken by averaging model 47- and 48-h data (Fig. 16a) shows that a major warm core of over  $8^\circ\text{C}$ , resulting from the upper-level west to northwesterly descending inflow, appears inside the RMW rather than near the eye center, as shown in Liu et al. (1999). As compared to the storm structures simulated 3 h earlier (cf. Figs. 16a and 8b), there are fewer mid- to upper-level clouds and organized updrafts near the western RMW axis, except for some associated with propagating gravity waves (Liu et al. 1999). Only some low-level clouds are present because of the subsidence warming and drying by the upper-level inflow. Of interest is that the subsidence-generated temperature gradients across the western RMW axis are even greater than those across the eastern RMW axis. Thus, one may view Bonnie as consisting of a cloud-free portion of the "pseudoe eyewall" and a cloudy portion of the eyewall. Of further interest is that despite the presence of the pronounced warm core to the west, the eye center tilts eastward closer to the vertical axis of the eastern RMW. The vertical tilt of the minimum pressure axis appears



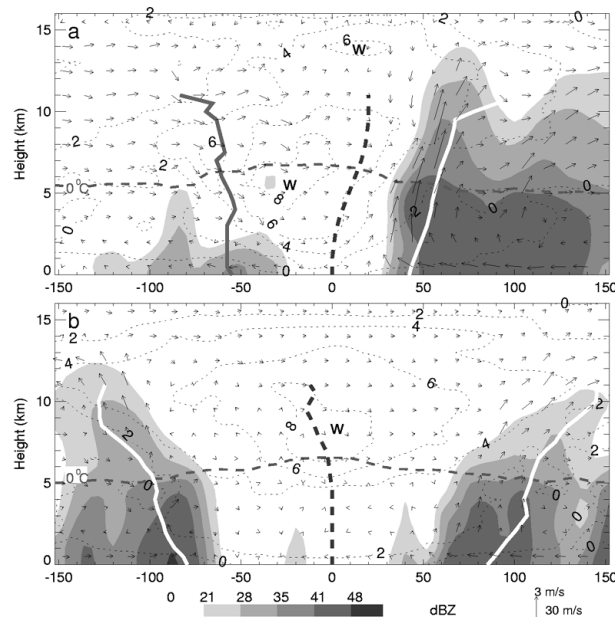


FIG. 16. As in Fig. 8b, but from the hourly average in (a) 47–48 and (b) 96–97 h that ends at 0000 UTC 24 and 0100 UTC 26 Aug 1998, respectively. The temperature deviations (dotted) are shown at intervals of 2°C. The center of the warm cores is denoted by the letter “W.”

to be more closely related to a warm core aloft (i.e., at  $z = 14$  km) that is generated by compensating subsidence associated with deep convection in the eastern eyewall.

During the maintenance stage, the storm moves away from the intense upper-level shearing environment (Fig. 9a) so that little organized inflow (and downdrafts) appears in the eyewall (Fig. 15c). As a result, weak to moderate updrafts with weak supergradient outflows are distributed in all quadrants, after upward motion is recovered in the western eyewall. Of particular interest is that while updrafts in the eyewall at this time are substantially weaker than those during the maturing stage (cf. Figs. 15b,c), the storm intensities at the two times are quite similar (see Fig. 3). This indicates that the hurricane intensity (in terms of the minimum surface pressures and maximum surface winds) may not be necessarily correlated to the intensity of deep convection (or updrafts) in the eyewall, even during a storm’s life cycle. This type of relationship was also found in observations, such as Hurricanes Gert (Willoughby et al. 1982) and Olivia (Black et al. 2002). It appears that some other factors may have to be considered in order to explain such a relationship.

In the present case, two such factors are the vertical thermal structures in the eye and Bonnie’s environmental conditions. To see the former point, a west–east vertical cross section through the storm center taken at 96 h is given in Fig. 16b, which shows updrafts and radar reflectivity of similar magnitudes in both the western and eastern eyewalls, and the distribution of a warm

core near the eye center with an upright vertical axis. They are in significant contrast to those shown in Fig. 16a. In addition, we see the development of weaker updrafts, more symmetries in the cross-sectional flow, and a greater RMW compared to those shown at 48 h (cf. Figs. 16a,b). Clearly, the vertical coherent warm-core structure assists the maintenance of a low pressure center below, whereas decreases in convective available potential energy, as the storm moves into a colder ocean surface, tend to support weak cloud development in the eyewall. The radial “expansion” of the eyewall could only explain the temporal weakening of the storm (cf. Figs. 3 and 14), which will be discussed in the next section.

## 7. Eyewall replacement and intensity changes

Because of its significance in hurricane intensity changes, the eyewall replacement processes have attracted considerable attention since the publication of Willoughby et al. (1982). A comparison of the observed and simulated reflectivity, given in Figs. 7, 8, and 14, appears to suggest the development of double eyewalls near 48 and 93 h. Because the storm’s inner-core structures change from highly asymmetric before 72 h to near axisymmetric afterward, we will present the model-simulated eyewall replacement scenarios during the 78–96-h period.

Figures 17 and 18a show how the eyewall evolves from a partial to double and a near-concentric eyewall during the eyewall replacement period. At 78 h, the storm still exhibits a partial “cloudy” eyewall “I,” as represented by the most intense reflectivity at  $R = 50$  km, that has moved from the northeast to north quadrant (Fig. 17a). Accompanied with the eyewall is an intense surface pressure gradient of greater than  $40 \text{ Pa km}^{-1}$  that coincides closely with the RMW. Of importance is that one outer spiral rainband “O” at  $R = 120$  km begins to propagate into the northwest to western quadrant as the large-scale descending inflow weakens. Similarly, more rainbands develop in the outer regions and propagate cyclonically into the northwestern quadrant.

Six hours later, the rainband I in the eyewall shrinks in width and radius, as do the outer rainbands (Figs. 17b and 18a). The outer rainbands O also intensify in terms of upward motion, local tangential winds, and surface pressure gradients as they move cyclonically inward. A secondary wind maximum, similar to that discussed by Samsury and Zipser (1995), starts to emerge at 87 h and  $R = 150$  km and intensifies with time as its RMW shrinks; they are consistent with the moderate deepening of the storm during the period (cf. Figs. 18a and 3). By 90 h, the inner eyewall becomes disintegrated with a few weak convective cells, and the inner RMW loses its characteristics starting from the surface (see Figs. 17c and 18a). But the most intense pressure gradients still remain underneath the eyewall (Fig. 17c), which is consistent with that shown in Zhang

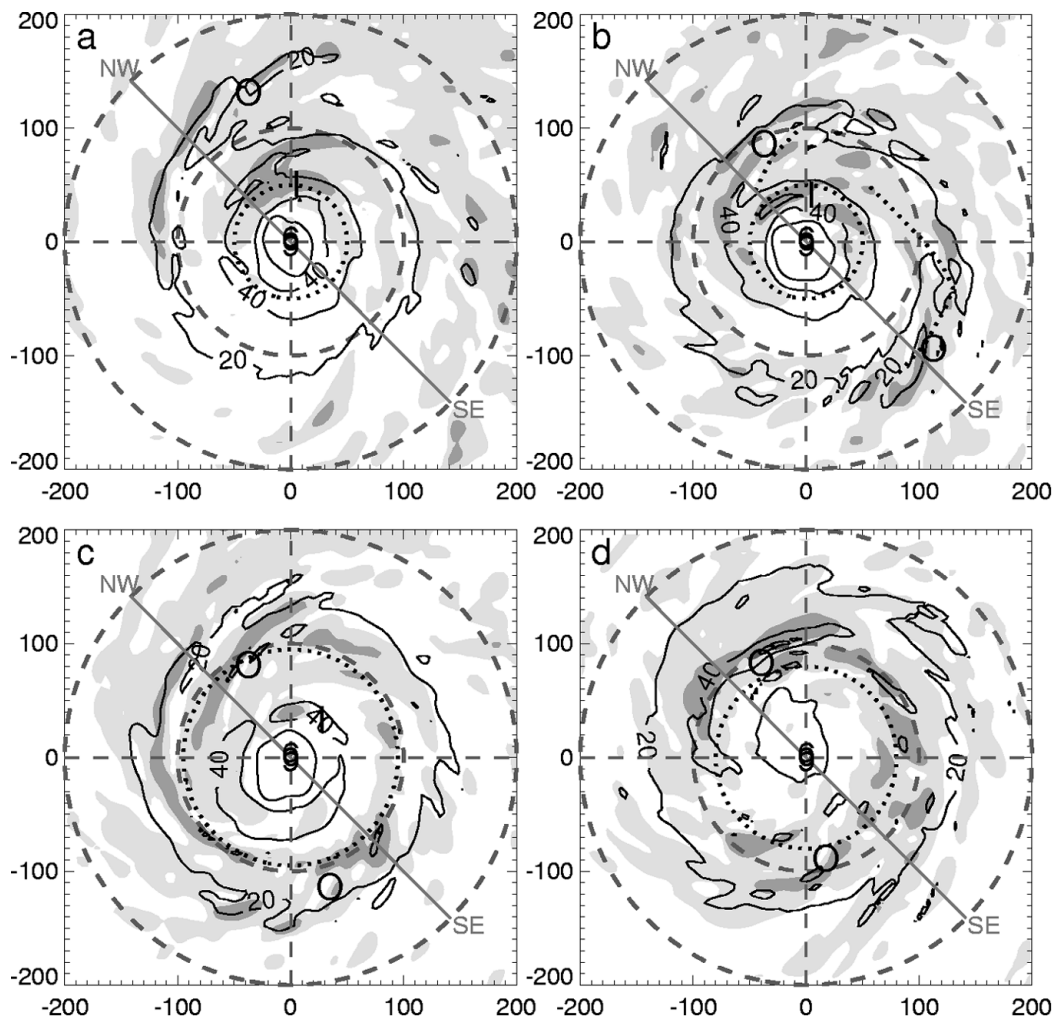


FIG. 17. Distribution of surface pressure gradient (i.e.,  $|\nabla p|$ ; solid) at intervals of  $20 \text{ Pa km}^{-1}$  and the layer (i.e., from the surface to 700 hPa) averaged reflectivities (shaded at 30 and 40 dBZ) from (a) 78-, (b) 84-, (c) 90-, and (d) 96-h simulations. Dotted lines denote the RMW or the axis of local wind maximum. Thick dashed lines are the radius of 100 and 200 km. Letters "O" and "I" denote the outer and inner rainbands, respectively. Line NW–SE represents the location of the vertical cross section shown in Fig. 18.

et al. (2001). On the other hand, the outer rainbands begin to form a full circle at  $R = 100 \text{ km}$ . Clearly, the outer rainbands O are energized at the expense of deep convection in the inner band I by consuming the high- $\theta_e$  air in the PBL that would be otherwise transported into the inner eyewall. At 96 h, the inner eyewall vanishes completely with few convective cells. Meanwhile, as the inner RMW disappears, the maximum surface pressure gradient shifts outward to  $R = 100 \text{ km}$  (cf. Figs. 17c,d), thus beginning the near-concentric eyewall stage with a much greater eye size. It takes less than 6 h to complete this eyewall replacement cycle. This phenomenon is similar to the so-called concentric eyewall cycle, as described by Willoughby et al. (1982). After the complete dissipation of the inner eyewall, the storm's intensification may resume. This is indeed the case during the maintenance stage of Bonnie (see Fig.

3). One can also notice that despite the rapid dissipation of the inner eyewall, little changes occur in the radial gradient of tangential flow (Fig. 18a). This clearly represents the slow manifold nature of (gradient) balanced flow in the eye.

Finally, Fig. 18b shows the vertical cross-sectional structures of the double RMWs or eyewalls during the transition period. Note the development of various perturbations in horizontal winds, each of which corresponds to a rainband. These perturbations result most likely from the locally enhanced pressure gradient force associated with latent heat release aloft. Of relevance here is the two local wind maxima ( $R_1$  and  $R_2$ ) associated with the two major rainbands (I and O). Their RMWs are generally located outside of the updraft core in the rainbands except in the PBL, which is consistent with the relationship between the eyewall and RMW shown

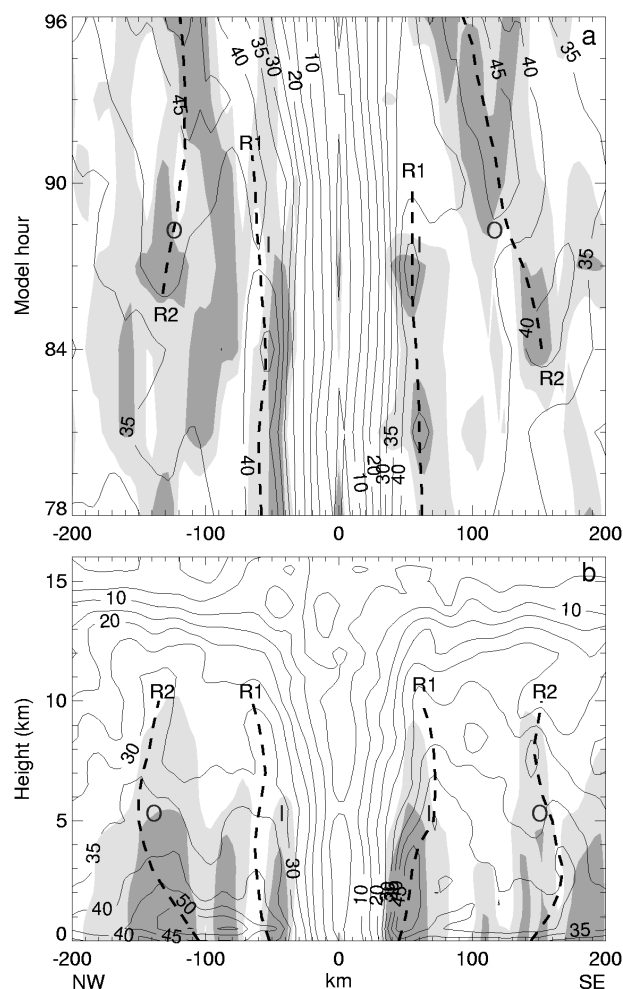


FIG. 18. (a) Time and NW-SE cross section of the horizontal wind speed at intervals of  $5 \text{ m s}^{-1}$  at  $z = 3 \text{ km}$  and (b) vertical cross section of the horizontal wind speed at intervals of  $5 \text{ m s}^{-1}$  along line NW-SE, given in Fig. 17, from the 87-h simulation. Shadings denote the simulated radar reflectivity at 30 and 40 dBZ and thick dashed lines denote the axes of the RMW. Letters "O" and "I" denote the outer and inner rainbands, respectively.

in Liu et al. (1999). At this time, the inner and outer rainbands are of similar intensity, but the former one weakens rapidly afterward, particularly for the southeastern rainband (Fig. 17). Because the flow within the inner RMW (i.e.,  $R_1$ ) is more inertially stable than that outside, it experiences little changes in intensity and structure with time (cf. Figs. 18a,b). In contrast, the outer RMW (i.e.,  $R_2$ ) tends to shrink in size, accounting for the deepening of the storm during the 84–96-h period (cf. Figs. 18a and 3).

## 8. Summary and conclusions

In this study, a 5-day explicit simulation of Hurricane Bonnie (1998) is performed using the MM5 with triply nested grids and the finest grid size of 4 km. This simulation covers an initial deepening stage with a partial

eyewall, a maintenance stage with eyewall replacements, and a partial landfall stage of the storm. The model initial and lateral boundary conditions are obtained from NCEP's global analysis, which is then enhanced by rawinsondes and surface observations. The initial hurricane vortex properties (i.e., temperature, winds, and moisture) are retrieved from the AMSU satellite data. The SST is updated daily, according to the TMI observations, to simulate the oceanic feedback under high wind conditions.

As verified against various observations and the best analysis, the 5-day simulation captures reasonably well the evolution and basic structures of the storm. The simulated track is within  $3^\circ$  latitude–longitude of the best track at the end of the 5-day integration, with the landfalling point close to the observed. However, the simulated storm appears to move faster than the observed, with the landfalling time about 15 h earlier than the observed. This could be attributed to the model's failure to capture Bonnie's slow-moving stage from 24 to 48 h, during which period the simulated track is too far to the west of the observed. The simulated intensity changes during the 5-day period compare favorably to the observed, including the marked deepening in the first 2 days and its subsequent maintenance stage with some intensity fluctuations. Nevertheless, the simulated intensity is about 8 hPa deeper than the observed after the first 2-day integration partly because of its propagation over an ocean surface that is about  $2^\circ\text{C}$  warmer than the observed and partly because of some deficiencies in the model physics. The MM5 also reproduces reasonably well the thermodynamic and dynamic structures in the eye and eyewall, as well as the structures and evolution of clouds and precipitation. They include the development of a partial eyewall, its replacement by a near-concentric eyewall with a greater eye size, and the eastward tilt of the hurricane circulations.

The effects of vertical wind shear on intensity changes and cloud asymmetries are examined using the model simulation, and can be described with the aid of Fig. 19, which shows a conceptual model of the eyewall evolution in the present case. We found that the storm-scale averaged vertical shear could not explain why Bonnie could deepen markedly with increasing vertical shear in the first 2 days. Our analysis shows the Bonnie could intensify because of the development of intense convection in the eastern eyewall with the high- $\theta_e$  air fed by a strong low-level southeasterly flow. Warm SST and the presence of a favorable large-scale flow aloft also appear to contribute indirectly to the deepening of the storm. In contrast, the existence of upper-level large-scale west to northwesterly (positive) shear tends to have detrimental impact on hurricane intensity. This vertical shear tends to suppress cloud development in the west semicircle through descending inflow of low- $\theta_e$  air, causing the warming and drying of the eyewall layers (Fig. 19a). This subsidence warming accounts for the generation of an intense warm core (e.g.,  $>8^\circ\text{C}$ ) inside,



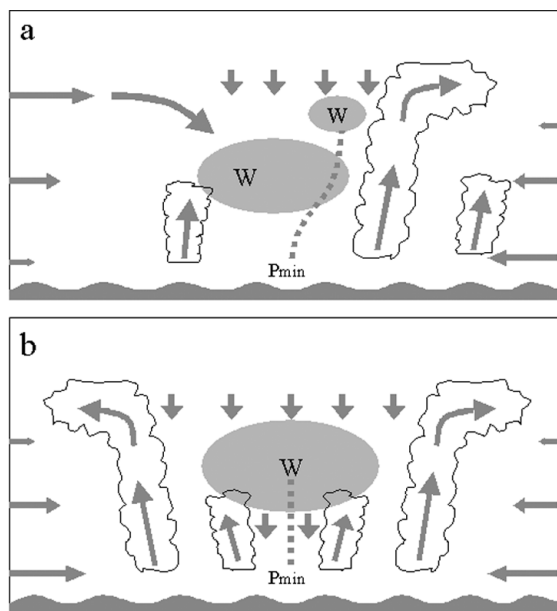


FIG. 19. A schematic conceptual model of the eyewall evolution during the two different development (i.e., intensifying and maintenance) stages in west–east vertical cross sections, showing the environmental vertical shear, the eyewall clouds, subsidence warming (with its core denoted by “W”), spiral rainbands, and the axes of updraft core (arrows) and minimum pressure (dashed).

but close to the western RMW axis with strong thermal gradients across. As a consequence, wavenumber-1 asymmetries in clouds and precipitation develop under the influences of negative vertical shear to the east and positive vertical shear to the west. This explanation does not contradict those found in previous studies, that is, with clouds and precipitation located on the downshear side (e.g., the northeastern quadrant in the present case).

It is shown that the RMW increases from about 50 to 100 km during the 78–90-h period. As indicated by both the simulation and observations, this radial expansion results from an eyewall replacement process (cf. Figs. 19a,b). It is found from the simulation that outer spiral rainbands, with new convective development, move into the west semicircle as the negative influence of the upper-level west to northwesterly shear diminishes after 72 h. As a result, the outer rainbands encircle at  $R > 100$  km around the inner eyewall and organize into a near-concentric outer eyewall (Fig. 19b). This new eyewall tends to prevent the high- $\theta_e$  air and angular momentum in the outer regions from being transported into the inner eyewall, thereby causing the rapid dissipation of deep convection in it. This process gives rise to the formation of double eyewalls during a 6-h transition period, each accompanied by a local wind maximum located outside of the updraft core in the rainbands except in the PBL. The storm weakens prior to and deepens after the eyewall replacement, which is consistent with the previous observational finding. The results indicate that the eyewall replacement phenomena

may have a certain degree of predictability because they appear to depend on the evolution of large-scale flows.

In part II of this series of papers, several sensitivity experiments will be conducted to examine the effects of various physical processes on the hurricane intensity and intensity changes and the development of cloud asymmetries, as well as the eyewall replacement process.

**Acknowledgments.** We would like to thank scientists at NASA GSFC and NOAA/AOML/HRD for providing the HAL/CAMEX3 observations on their Web sites, which allowed us to verify our model simulation. Thanks also go to Dr. Xiaofan Li at NOAA/NESDIS/ORA for his assistance in obtaining the TMI SST data, and to Bill Frank of The Pennsylvania State University for his useful discussion on the effects of vertical wind shear. The first author has benefited from many discussions with and assistance from Dave Yanuk, Xingbao Wang, Min Wei, Weizhong Zheng, and Xiaoxue Wang. This work was supported by NSF Grant ATM-9802391, NASA Grants NAG-57842 and NAG-510746, Navy/ONR, and NOAA/NESDIS.

#### REFERENCES

- Anthes, R. A., 1982: *Tropical Cyclones: Their Evolution, Structure and Effects*. Meteor. Monogr., No. 41, Amer. Meteor. Soc., 208 pp.
- Avila, L. A., cited 1998: Hurricane Bonnie Preliminary Report 19–30 August 1998. [Available online at <http://www.nhc.noaa.gov/1998bonnie.html>.]
- Bender, M., 1997: The effect of relative flow on the asymmetric structure in the interior of hurricanes. *J. Atmos. Sci.*, **54**, 703–724.
- Black, M. L., J. E. Gamache, F. D. Marks Jr., C. E. Samsury, and H. E. Willoughby, 2002: Eastern Pacific Hurricanes Jimena of 1991 and Olivia of 1994: The effect of vertical shear on structure and intensity. *Mon. Wea. Rev.*, **130**, 2291–2312.
- Bracken, W. E., and L. F. Bosart, 2000: The role of synoptic-scale flow during tropical cyclogenesis over the North Atlantic Ocean. *Mon. Wea. Rev.*, **128**, 353–376.
- Burpee, R. W., and M. L. Black, 1989: Temporal and spatial variations of rainfall near the centers of two tropical cyclones. *Mon. Wea. Rev.*, **117**, 2204–2218.
- Chelton, D. B., F. J. Wentz, C. L. Gentemann, R. A. de Szoeke, and M. G. Schlax, 2000: Satellite microwave SST observations of transequatorial tropical instability waves. *Geophys. Res. Lett.*, **27**, 1239–1242.
- Corbosiero, K. L., and J. Molinari, 2002: The effects of vertical wind shear on the distribution of convection in tropical cyclones. *Mon. Wea. Rev.*, **130**, 2110–2123.
- DeMaria, M., 1996: The effect of vertical shear on tropical cyclone intensity change. *J. Atmos. Sci.*, **53**, 2076–2087.
- Dudhia, J., 1993: A nonhydrostatic version of the Penn State–NCAR mesoscale model: Validation tests and simulation of an Atlantic cyclone and cold front. *Mon. Wea. Rev.*, **121**, 1493–1513.
- Elsberry, R. L., and R. A. Jeffries, 1996: Vertical wind shear influences on tropical cyclone formation and intensification during TCM-92 and TCM-93. *Mon. Wea. Rev.*, **124**, 1374–1387.
- Frank, W. M., and E. A. Ritchie, 1999: Effects of environmental flow upon tropical cyclone structure. *Mon. Wea. Rev.*, **127**, 2044–2061.
- , and —, 2001: Effects of vertical wind shear on hurricane intensity and structure. *Mon. Wea. Rev.*, **129**, 2249–2269.



- Franklin, J. L., S. J. Lord, and F. D. Marks Jr., 1988: Dropwindsonde and radar observations of the eye of Hurricane Gloria (1985). *Mon. Wea. Rev.*, **116**, 1237–1244.
- , —, S. E. Feuer, and F. D. Marks Jr., 1993: The kinematic structure of Hurricane Gloria (1985) determined from nested analyses of dropwindsondes and Doppler radar data. *Mon. Wea. Rev.*, **121**, 2433–2451.
- Gray, W. M., 1968: Global view of the origin of tropical disturbances and storms. *Mon. Wea. Rev.*, **96**, 669–700.
- Grell, G. A., J. Dudhia, and D. R. Stauffer, 1995: A description of the fifth generation Penn State/NCAR mesoscale model (MM5). NCAR Tech. Note NCAR/TN-398 + STR, 138 pp. [Available from NCAR Publications Office, P. O. Box 3000, Boulder, CO 80307-3000.]
- Heymsfield, G. M., J. B. Halverson, J. Simpson, L. Tian, and T. P. Bui, 2001: ER-2 Doppler radar investigations of the eyewall of Hurricane Bonnie during the convection and moisture experiment-3. *J. Appl. Meteor.*, **40**, 1310–1330.
- Hong, X., S. W. Chang, S. Raman, L. K. Shay, and R. Hodur, 2000: The interaction between Hurricane Opal (1995) and a warm core ring in the Gulf of Mexico. *Mon. Wea. Rev.*, **128**, 1347–1365.
- Kain, J. S., and J. M. Fritsch, 1993: Convective parameterization for mesoscale models: The Kain–Fritsch scheme. *The Representation of Cumulus Convection in Numerical Models*, Meteor. Monogr., No. 46, Amer. Meteor. Soc., 165–170.
- Liu, Y., D.-L. Zhang, and M. K. Yau, 1997: A multiscale numerical study of Hurricane Andrew (1992). Part I: Explicit simulation and verification. *Mon. Wea. Rev.*, **125**, 3073–3093.
- , —, and —, 1999: A multiscale numerical study of Hurricane Andrew (1992). Part II: Kinematics and inner-core structures. *Mon. Wea. Rev.*, **127**, 2597–2616.
- Marks, F. D., Jr., R. A. Houze Jr., and J. F. Gamache, 1992: Dual-aircraft investigation of the inner core of Hurricane Norbert. Part I: Kinematic structure. *J. Atmos. Sci.*, **49**, 919–942.
- Miller, B. L., 1958: Rainfall rates in Florida hurricanes. *Mon. Wea. Rev.*, **86**, 258–264.
- Pasch, R. J., L. A. Avila, and J. L. Guiney, 2001: Atlantic hurricane season of 1998. *Mon. Wea. Rev.*, **129**, 3085–3123.
- Ritchie, E. A., and R. L. Elsberry, 2001: Simulations of transformation stage of the extratropical transition of tropical cyclones. *Mon. Wea. Rev.*, **129**, 1462–1480.
- Rogers, R. F., S. S. Chen, J. E. Tenerelli, and H. Willoughby, 2003: A numerical study of the impact of vertical shear on the distribution of rainfall in Hurricane Bonnie (1998). *Mon. Wea. Rev.*, **131**, 1577–1599.
- Samsury, C. E., and E. J. Zipser, 1995: Secondary wind maxima in hurricanes: Airflow and relationship to rainbands. *Mon. Wea. Rev.*, **123**, 3502–3517.
- Sauvageot, H., 1992: *Radar Meteorology*. Artech House, 366 pp.
- Shapiro, L. J., 1983: Asymmetric boundary layer flow under a translating hurricane. *J. Atmos. Sci.*, **40**, 1984–1998.
- Tao, W.-K., and J. Simpson, 1993: The Goddard cumulus ensemble model. Part I: Model description. *Terr. Atmos. Oceanic Sci.*, **4**, 35–72.
- Willoughby, H. E., J. A. Clos, and M. G. Shoreibah, 1982: Concentric eye walls, secondary wind maxima, and the evolution of the hurricane vortex. *J. Atmos. Sci.*, **39**, 395–411.
- , F. D. Marks, and R. J. Feinberg, 1984: Stationary and moving convective bands in hurricanes. *J. Atmos. Sci.*, **41**, 3189–3211.
- Zhang, D.-L., and R. A. Anthes, 1982: A high-resolution model of the planetary boundary layer—Sensitivity tests and comparisons with SESAME-79 data. *J. Appl. Meteor.*, **21**, 1594–1609.
- , Y. Liu, and M. K. Yau, 2000: A multiscale numerical study of Hurricane Andrew (1992). Part III: Dynamically induced vertical motion. *Mon. Wea. Rev.*, **128**, 3772–3788.
- , —, and —, 2001: A multiscale numerical study of Hurricane Andrew (1992). Part IV: Unbalanced flows. *Mon. Wea. Rev.*, **129**, 92–107.
- , —, and —, 2002: A multiscale numerical study of Hurricane Andrew (1992). Part V: Inner-core thermodynamics. *Mon. Wea. Rev.*, **130**, 2745–2763.
- Zhu, T., D.-L. Zhang, and F. Weng, 2002: Impact of the Advanced Microwave Sounding Unit measurements on hurricane prediction. *Mon. Wea. Rev.*, **130**, 2416–2432.